Int J Adv Manuf Technol (2013) 67:501–516
DOI 10.1007/s00170-012-4501-9

ORIGINAL ARTICLE

Stability analysis for the crankshaft grinding machine subjected to a variable-position worktable

K. C. Cha · N. Wang · J. Y. Liao

Received: 18 January 2012 / Accepted: 5 September 2012 / Published online: 30 September 2012

Abstract This paper serves to evaluate the dynamic performance and the cutting stability of the crankshaft grinding machine. The governing equations for the 7 degrees of freedom (DOF) lumped-mass model are formulated by the Lagrange energy method. The absolute value of the maximum negative real part of the overall dynamic compliance (MNRPODC) and the limiting chip width are the main performance indicators used to explore the structure's dynamic characteristics and the cutting stability of the grinding machine in various worktable positions. The effect on system performance of the distance between the mass center of the workpiece and the worktable module in the z direction is also analyzed. Based on the stability theory for regenerative chatter model, a computer program has been developed that utilizes the three-dimensional stability lobe diagrams of the multi-DOF system to automatically identify the stable and chatter zones. Time domain simulation of the cutting conditions is used to verify the stability lobe diagrams. Finally, an optimization analysis utilizing the particle swarm optimization method is carried out to obtain the optimal design variables. The results, in terms of |MNRPODC| or the limiting critical chip width, show improvements by a factor of 6.5 and are superior to that of the prototype machine.

K. C. Cha (✉) · N. Wang
Department of Mechanical Engineering, Chang Gung University,
259 Wen-Hwa 1st Road, Kwei-Shan, Tao-Yuan, Taiwan,
Republic of China
e-mail: ckc001@mail.cgu.edu.tw

N. Wang
e-mail: nenzi001@mail.cgu.edu.tw

J. Y. Liao
Chung-Shan Institute of Science and Technology,
Long-Tan, Tao-Yuan, Taiwan, Republic of China
email: liaojenyi@gmail.com

Keywords Crankshaft grinding machine · State space approach · Dynamic compliance · Regenerative chatter model · Stability lobe diagram · Particle swarm optimization

1 Introduction

Chatter resulting from self-excitation during machining has to be eliminated or minimized in machine tools. Chatter is highly detrimental to tool life and surface finish and is usually accompanied by considerable noise. The chatter mechanism is capable of modulating a steady, nonperiodic external energy source and generating a periodic force through the vibration of the system such that it sustains the unwanted vibration; hence, it is a self-exciting chatter. If the chip width is large with respect to the dynamic stiffness of the system, the chatter would start and grow quickly. Chatter also adversely affects the rate of production and, in many cases, its elimination can only be achieved by reducing the material removal rates. Thus, an effective approach to the understanding of the performance and stability of machine tools is an important subject in practice.

Adjustment of the cutting process and modification of the machining structure are two approaches to study chatter behavior in machining. In the first approach, the stability lobe diagram that predicts the onset of chatter is used to determine the limiting chip width ($b_{\lim}$) and spindle speed to avoid chatter. Examples include the early work by Tobias and Fishwick [1], Tlusty and Polacek [2], as well as Koenigsberger and Tlusty [3]. Later, Altintas and Budak [4] introduced a chatter theory that can be applied to generate lobe diagrams for linear systems. Tlusty and Ismail [5] revealed that nonlinearities such as the tool jumping out of cut, multiple regeneration, process damping, and a nonlinear cutting constant are negligible in linear stability analysis. Schmitz [6] conducted a study dealing with the automatic trimming of machining stability lobes by using a script in AutoCad. In the second approach, the structure of the machine is modified to improve its dynamic properties. Many

studies on the stiffness or structural vibrations of machine tools were conducted by experimental, analytical, or numerical methods in the past decades. Among them, Yoshimura [7, 8] achieved highly fruitful results. In 2004, Altintas and Weck [9] summarized the state of knowledge in the dynamics of metal cutting and grinding operations. They believed that an analytic description of the dynamic behavior of grinding processes was difficult to achieve because of the complexity of the contact conditions. They also agreed that frequency and time domain simulation models were effective tools to improve machine tool design and for optimal planning of machining operations. In 2008 and 2011, Cha et al. [10, 11] proposed a structural stability prediction model of a surface grinder using a backpropagation neural network and studied the stability analysis for a surface grinder in various worktable positions. The latter is a rarely seen study. Some other works and the related theory can be found in refs. [12, 13].

In regenerative chatter theories, the stability of the process can be analyzed using the Nyquist stability criterion. One can express $b_{\lim}$ as a function of the specific dynamic cutting stiffness K_f and the real part of the frequency response $R_e[G(\omega)]$. If the chip width b_w is large compared with $b_{\lim}$, chatter will occur and only the negative real part of the frequency response will cause chatter. In addition, the critical parameter $b_{\lim}$ ($b_{\lim,cr}$) is inversely proportional to the absolute value of the maximum negative real part of the overall dynamic compliance ($|MNRPODC|$) [10, 11]. If the chip width is less than $b_{\lim,cr}$, no chatter will occur regardless of the spindle speed. Therefore, the smaller the $|MNRPODC|$, the larger the $b_{\lim,cr}$ will be. In a machining process, the position of the worktable varies, which means that the machine structure or stability is also changed. In this study, the |MNRPODC| and $b_{\lim}$ are the main performance indicators used to evaluate the crankshaft grinding machine structure's dynamic performance and cutting stability in various worktable positions. Similar to the author's study in ref. [11], a helpful design technique is provided for the assessment of structural dynamic performance that is useful for developing or designing a new machine tool.

2 Basic theory

The crankshaft grinding machine is similar to an external grinder. The schematic of an external grinder using traverse motion is shown in Fig. 1. The workpiece is supported and rotated between centers. The headstock provides the low speed rotational drive to the workpiece and is mounted, together with the tailstock, on a worktable that is moved horizontally (z motion) using a hydraulic drive. The grinding wheel spindle is horizontal and parallel to the axis of workpiece rotation, and a horizontal hydraulic feed can be applied to the wheel head in a direction normal to the axis of workpiece rotation (x motion); this motion is known as infeed.

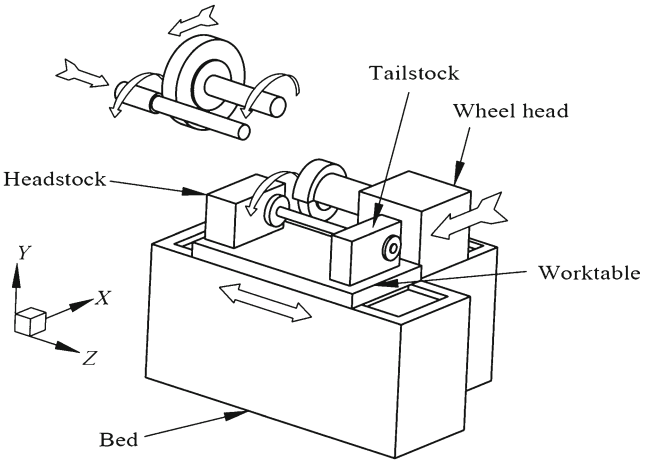

Fig. 1 The schematic of an external grinder and defined coordinate system

In this study, based on the lumped parameter model of an M8620 crankshaft grinder with excellent experimental proof proposed by Zheng et al. [14], the crankshaft grinding machine with 7 degrees of freedom (DOF) (x_1, x_2, θ_2, x_3, θ_3, x_4, θ_4) dynamic model and analysis in various worktable positions are presented in Fig. 2. The main parts in the system consist of the wheel stock, the spindle module, workpiece, and the worktable module. The spindle module includes the grinding wheel, the wheel axle, and the belt wheel. The worktable module includes the head stock, the worktable, and the tail stock. Considering the fact that the direction of the force which affects the processing accuracy most severely is in the horizontal direction, the horizontal direction is adopted as the x coordinate of the system (model view from top in Fig. 1). The structure of the bed is considered to be fixed when the worktable module is at a specific position L_z. New parameters are formed if the position of the worktable module is changed.

The above 7 degrees of freedom can be separately denoted as:

- x_1 Displacement of the mass center of the wheel stock (in meter)
- x_2 Displacement of the mass center of the spindle module (in meter)
- θ_2 Angular displacement of mass center of the spindle module (in radian)
- x_3 Displacement of the mass center of the workpiece (in meter)
- θ_3 Angular displacement of mass center of the workpiece (in radian)
- x_4 Displacement of the mass center of the worktable module (in meter)
- θ_4 Angular displacement of mass center of the worktable module (in radian)

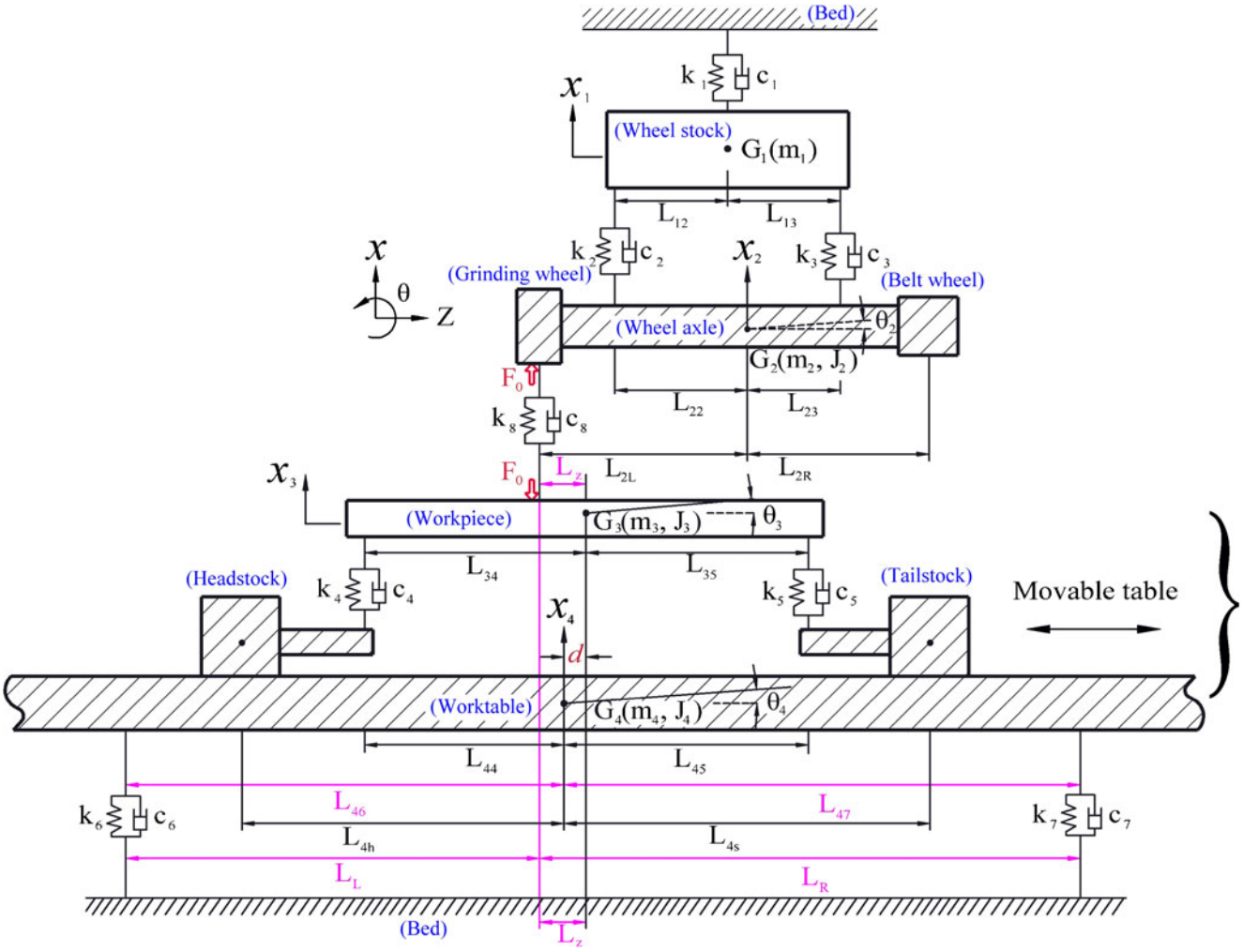

Fig. 2 The lumped-mass modeling with the worktable position variations of a crankshaft grinding machine

2.1 Modeling and formulation

The origin of the z coordinate in the system (Fig. 2) is at L_z=0. In the following section, the dynamic equations of the system are formulated in accordance with the Lagrange energy method. The kinetic energy T, potential energy U, and damping dissipated energy V, of the system are

$$
\begin{aligned}
T &= \tfrac{1}{2}\sum_{j=1}^{7}\left(m_j\dot{x}_j^{\,2} + J_j\dot{\theta}_j^{\,2}\right) = \tfrac{1}{2}\,m_1\dot{x}_1^2 + \tfrac{1}{2}(m_2+m_L+m_R)\dot{x}_2^2 + \tfrac{1}{2}\left[J_2 + m_L\times(L_{2L})^2 + m_R\times(L_{2R})^2\right]\dot{\theta}_2^2 + \tfrac{1}{2}m_3\dot{x}_3^2 + \tfrac{1}{2}J_3\,\dot{\theta}_3^2 \\
&\quad + \tfrac{1}{2}(m_4+m_h+m_s)\dot{x}_4^2 + \tfrac{1}{2}\left[J_4 + m_h\times(L_{4h})^2 + m_s\times(L_{4s})^2\right]\dot{\theta}_4^2 \\
U &= \tfrac{1}{2}\sum_{j=1}^{7}\left(k_j x_j^2\right) = \tfrac{1}{2}k_1x_1^2 + \tfrac{1}{2}\,k_2[(x_1-(x_2-L_{22}\times\theta_2)]^2 + \tfrac{1}{2}\,k_3[(x_1-(x_2+L_{23}\times\theta_2)]^2 + \tfrac{1}{2}k_8[(x_2-L_{2L}\times\theta_2)-(x_3-L_Z\times\theta_3)]^2 \\
&\quad + \tfrac{1}{2}k_4[(x_3-L_{34}\times\theta_3)-(x_4-L_{44}\times\theta_4)]^2 + \tfrac{1}{2}k_5[(x_3+L_{35}\times\theta_3)-(x_4+L_{45}\times\theta_4)]^2 + \tfrac{1}{2}k_6[(x_4-L_{46}\times\theta_4)]^2 + \tfrac{1}{2}k_7[(x_4+L_{47}\times\theta_4)]^2 \\
V &= \tfrac{1}{2}\sum_{j=1}^{7}\left(c_j\dot{x}_j^{\,2}\right) = \tfrac{1}{2}c_1\dot{x}_1^2 + \tfrac{1}{2}c_2\left[\left(\dot{x}_1-\left(\dot{x}_2-L_{22}\times\dot{\theta}_2\right)\right)\right]^2 + \tfrac{1}{2}c_3\left[\left(\dot{x}_1-\left(\dot{x}_2+L_{23}\times\dot{\theta}_2\right)\right)\right]^2 + \tfrac{1}{2}c_8\left[\left(\dot{x}_2-L_{2L}\times\dot{\theta}_2\right)-\left(\dot{x}_3-L_Z\times\dot{\theta}_3\right)\right]^2 \\
&\quad + \tfrac{1}{2}c_4\left[\left(\dot{x}_3-L_{34}\times\dot{\theta}_3\right)-\left(\dot{x}_4-L_{44}\times\dot{\theta}_4\right)\right]^2 + \tfrac{1}{2}c_5\left[\left(\dot{x}_3+L_{35}\times\dot{\theta}_3\right)-\left(\dot{x}_4+L_{45}\times\dot{\theta}_4\right)\right]^2 + \tfrac{1}{2}c_6\left[\left(\dot{x}_4-L_{46}\times\dot{\theta}_4\right)\right]^2 \\
&\quad + \tfrac{1}{2}c_7\left[\left(\dot{x}_4+L_{47}\times\dot{\theta}_4\right)\right]^2
\end{aligned}
\tag{1}
$$

Substituting Eq. 1 into Lagrange's Eq. 2, where:

$$\frac{d}{dt}\left(\frac{\partial T}{\partial \dot{x}_j}\right)+\frac{\partial U}{\partial x_j}+\frac{\partial V}{\partial \dot{x}_j}=f_j\ \ (j=1,\ 2,\ldots,\ 7). \tag{2}$$

The dynamic equations of the structure under force in matrix form can be expressed as follows:

$$[M]_{7\times7}\left\{\ddot{x}(t)\right\}_{7\times1}+[C]_{7\times7}\left\{\dot{x}(t)\right\}_{7\times1} +[K]_{7\times7}\{x(t)\}_{7\times1}=\{f\}_{7\times1}e^{j\omega t}. \tag{3}$$

2.2 System matrices

After rearranging, we obtain the following expressions for the mass matrix $[M]_{7\times7}$, the stiffness matrix $[K]_{7\times7}$, and damping matrix $[C]_{7\times0}$:

1. Mass matrix $[M]_{7\times7}$

$$\begin{aligned}
m_{11}&=m_1\\
m_{22}&=m_2+m_L+m_R\\
m_{33}&=J_2+m_L\times(L_{2L})^2+m_R\times(L_{2R})^2\\
m_{44}&=m_3\\
m_{55}&=J_3\\
m_{66}&=m_4+m_h+m_s\\
m_{77}&=J_4+m_h\times(L_{4h})^2+m_s\ \times(L_{4s})^2
\end{aligned}$$

The other elements are zero in value.

2. Stiffness matrix $[K]_{7\times7}$

$$\begin{aligned}
k_{11}&=k_1+k_2+k_3\\
k_{21}&=k_{12}=-k_2-k_3\\
k_{22}&=k_2+k_3+k_8\\
k_{31}&=k_{13}=L_{22}\times k_2-L_{23}\times k_3\\
k_{32}&=k_{23}=-L_{22}\times k_2+L_{23}\times k_3-L_{2L}\times k_8\\
k_{33}&=L_{22}\times L_{22}\times k_2+L_{23}\times L_{23}\times k_3+L_{2L}\times L_{2L}\times k_8\\
k_{42}&=k_{24}=-k_8\\
k_{43}&=k_{34}=L_{2L}\times k_8\\
k_{44}&=k_8+k_4+k_5\\
k_{52}&=k_{25}=L_z\times k_8\\
k_{53}&=k_{35}=-L_z\times L_{2L}\times k_8\\
k_{54}&=k_{45}=-L_z\times k_8-L_{34}\times k_4+L_{35}\times k_5\\
k_{55}&=L_z\times L_z\times k_8+L_{34}\times L_{34}\times k_4+L_{35}\times L_{35}\times k_5\\
k_{64}&=k_{46}=-k_4-k_5\\
k_{65}&=k_{56}=L_{34}\times k_4-L_{35}\times k_5\\
k_{66}&=k_4+k_5+k_6+k_7\\
k_{74}&=k_{47}=L_{44}\times k_4-L_{45}\times k_5\\
k_{75}&=-L_{44}\times L_{34}\times k_4-L_{45}\times L_{35}\times k_5\\
k_{76}&=k_{67}=-L_{44}\times k_4+L_{45}\times k_5-L_{46}\times k_6+L_{47}\times k_7\\
k_{77}&=L_{44}\times L_{44}\times k_4+L_{45}\times L_{45}\times k_5+L_{46}\times L_{46}\times k_6\\
&\quad+L_{47}\times L_{47}\times k_7
\end{aligned}$$

The other elements are zero in value. The relation holds for $L_{46}=L_L+L_z-d$ and $L_{47}=L_R-L_z+d$, where d is the distance between the mass center of the workpiece and the worktable module in the z direction. L_z is the displacement of the workpiece to the origin. The location to the right of the original position is a positive value, while the reverse condition is a negative value.

3. *Damping matrix* $[C]_{7\times7}$: Within this system, the damping is assumed to be proportional. The types of both the damping matrix and the stiffness matrix are the same. By changing the k in the stiffness matrix to c, the damping matrix is formulated.
4. *Force vector* $\{f\}_{7\times1}$: A more detail description will be given in Section 2.4. The equivalent force vector is $f^T=[0\ \ 1\ -L_{2L}\times1\ -1\quad L_z\times1\quad 0\quad 0]$ in Eq. 3.

So far, the formulation of the lumped-mass modeling for a crankshaft grinding machine of 7 DOF has been done using the energy method. Subsequently, the state space method is used for further analysis.

2.3 State space approach

As discussed in Gawronski's text [15], there are several forms of state space modal models. In the following a hybrid modal state space approach is used in which the system states are modal (displacements and velocities), but the input and outputs are in generalized coordinates. In this study, Eq. 3 can be transformed in the state space model as follows. If the state variables and input vector are selected as Eq. 4, the following state equation and output equation for the system are obtained:

$$\begin{aligned}
&\{u\}_{14\times1}=\begin{Bmatrix}x\\ \dot{x}\end{Bmatrix};\ \{x\}_{7\times1}=[x_1,\quad x_2,\quad \theta_2,\quad x_3,\quad \theta_3,\quad x_4,\quad \theta_4]^T;\\
&\{f\}_{7\times1}=[0,\quad 1\quad -L_{2L}\times1,\quad -1,\quad L_Z\times1,\quad 0\quad 0]^T.
\end{aligned} \tag{4}$$

The state equations are

$$\{\dot{u}\}_{14\times1}=[A_c]_{14\times14}\{u(t)\}_{14\times1}+[B_c]_{14\times7}\{f\}_{7\times1} \tag{5}$$

$$\begin{aligned}
\{r(t)\}_{1\times1}&=(x_2-L_{2L}\times\theta_2)-(x_3-L_z\times\theta_3)=\{f\}_{1\times7}^T\{x\}_{7\times1}\\
&=\begin{bmatrix}f^T & 0\end{bmatrix}_{1\times14}\{u\}_{14\times1}=[C_c]_{1\times14}\{u\}_{14\times1.}
\end{aligned} \tag{6}$$

Thus,

$$[A_c]=\begin{bmatrix}0 & I\\ -M^{-1}K & -M^{-1}C\end{bmatrix},\ [B_c]=\begin{bmatrix}0\\ M^{-1}f\end{bmatrix},\ [C_c]=\begin{bmatrix}f^T & 0\end{bmatrix},\ [D_c]=[0].$$

If the Δt is the first order hold sampling time step, the vectors can be discretized as

$$\{u_k\} = \begin{Bmatrix} x_k \\ \dot{x}_k \end{Bmatrix} = \begin{Bmatrix} x(k\Delta t) \\ \dot{x}(k\Delta t) \end{Bmatrix}; \{f_k\} = \{f(k\Delta t)\}; \{y_k\} = \{y(k\Delta t)\}; \tag{7}$$

The equations can then be transformed from a continuous-time model to a discrete-time model as follows:

$$\begin{aligned} \{u_{k+1}\} &= [A]_{2\,N\times 2N}\{u_k\} + [B]_{2N\times 2N}\{f_k\}; \\ \{y_k\} &= [C]_{N\times 2N}\{u_k\} + [D]_{N\times N}\{f_k\}; \\ [A] &= e^{[A_c]\Delta t}; \\ [B] &= \int_0^{\Delta t} e^{[A_c]\cdot\tau} d\tau \times [B_c] = [A-I][A_c]^{-1}[B_c],\ or \\ [B] &= \tfrac{1}{\Delta t}\left([A-I][A_c]^{-1}\right)^2[B_c]. \end{aligned} \tag{8}$$

The above equations can apply to a time response analysis and to a time variant nonlinear system.

2.4 Dynamic compliance calculation

In this system, when the mass center of a worktable is moved to an arbitrary position, the calculation of the dynamic compliance between the grinding wheel and the workpiece is acted upon by a unit harmonic force in the opposite direction to that imposed on the position, in response to the related degree of freedom [16]. The equivalent force is depicted as $f^T = [0 \quad 1 \quad -L_{2L}\times 1 \quad -1 \quad L_z \times 1 \quad 0 \quad 0]$ in Eq. 4. In addition, based on the aforementioned theory, the A_c, B_c, C_c, and D_c in the state space equations are formed and the response for x_2, x_3, θ_2, and θ_3 are calculated. The equivalent dynamic compliance between the grinding wheel and the workpiece is obtained by $r(t) = (x_2 - L_{2L}\times\theta_2) - (x_3 - L_z\times\theta_3)$. The oriented transfer function $G(\omega)$ was established between the cutting force and the normal displacement to the cut. The complex form of dynamic compliance in the frequency domain can be partitioned into real and imaginary parts. The real part $R_e[G(\omega)]$ and the imaginary part $\mathrm{Im}[G(\omega)]$ can be used to draw a Nyquist diagram. Thereafter, it is possible to determine the extents of system stability by inspecting the absolute values of the maximum negative real part. It is also an important basic reference in the study of cutting stability [9–13, 16].

To obtain an accurate solution of |MNPRODC| as well as for efficient computation, the "freqgrid" function in the Matlab toolbox is used for automatically generating a frequency grid for a frequency response. The generated frequency grids are denser around the resonant frequency and the antiresonant frequency. In this study, the grid density around the first mode is approximately 40 times higher than the general case.

2.5 Stability analysis of regenerative chatter vibration

Similar to metal cutting, the main source of the self-excited chatter vibrations in grinding is also due to a regenerative effect. Because of the complexity of the contact conditions, an analytic description of the dynamic behavior of grinding processes is difficult to achieve. It is assumed that the speed of the grinding wheel is much faster than the speed of the workpiece. The operation of the crankshaft grinding machine can be likened to cylindrical turning where the single point cutting tool is replaced by a grinding wheel. The general relationships for the dynamic behavior of orthogonal metal cutting and chatter stability lobes in a regeneration model are provided as follows. In this study, these relationships are still valid as in ref. [11].

The principle behind the occurrence of regenerative chatter is instability due to time lag. In a metal cutting operation, the current vibration, $x(t)$, between tool and workpiece as opposing points in the machine structure causes the tool to cut into the wavy surface $x(t-\tau)$ of the previous pass; the variable chip thickness between the two causes a variation of the cutting force $F(t)$ that, in a feedback fashion, causes vibration $x(t)$. The general dynamic chip thickness can be expressed as follows:

$$h(t) = h_0 - [x(t) - x(t-\tau)] \tag{9}$$

where h_0 is the intended chip thickness, which is equal to the feed rate of the machine. Assuming the force is proportional to the cutting constant in the feed direction (K_f), the width of cut b_w, and the dynamic chip load, the cutting force equation can be expressed as:

$$F(t) = K_f b_w h(t) = K_f b_w [h_0 - x(t) + x(t-\tau)] \tag{10}$$

where K_f is also called the specific cutting force per area ($b_w h$). The value of K_f can be found in refs. [12, 13].

The system can be illustrated as in ref. [11] by the block diagram, where the parameters of the dynamic cutting process can be represented in the Laplace domain. Input to the system is the desired chip thickness h_0, and the output of the feedback system is the current vibration, $x(t)$, left on the inner surface. In the Laplace domain, $x(s)=\pounds[x(t)]$, and the vibration induced on the outer surface during the previous revolution is $e^{-\tau s}x(s)=\pounds[x(t-\tau)]$, where τ is the spindle period (period between two cuts). The dynamic chip thickness in the Laplace domain is

$$h(s) = h_0 - x(s) + e^{-\tau s}x(s) = h_0 + (e^{-\tau s} - 1)x(s) \tag{11}$$

which produces a dynamic cutting force of

$$F(s) = K_f b_w h(s). \tag{12}$$

The cutting force excites the structure and produces the current vibrations

$$x(s) = F(s)G(s) = K_f b_w h(s)G(s) \tag{13}$$

where $G(s)$ is the oriented transfer function of the vibratory system.

The chatter stability lobes and the related spindle speed for a single point machining operations are provided as [16]:

$$b_{\lim} = \frac{-1}{2K_f R_e(G)}, \frac{f_c}{\Omega} = N + \frac{\varepsilon}{2\pi}, \varepsilon = 2\pi - 2\tan^{-1}\left[\frac{R_e[G(\omega)]}{\mathrm{Im}[G(\omega)]}\right] \tag{14}$$

In Eq. 14, K_f is the specific cutting force in newtons per square millimeter, depending on material used [16]. $b_{\lim}$ is the limiting chip width to avoid chatter, f_c is the chatter frequency in hertz, and Ω is the spindle speed in revolutions per second. N is the largest possible integer such that $\varepsilon/(2\pi)<1$. ε is the phase (in radian) between current and previous tool vibrations.

When the stability lobe diagram increases in complexity, most scholars ignore the interaction between the stable and unstable zones of intersection lobes [17]. In the end milling of thin-walled plates, due to the change of cutting position, mass, and stiffness of cutting system and other factors, the two-dimensional stability lobe diagram sometimes is not comprehensive to describe the stability of chatter system. Therefore, the 3D lobe diagram construction for the dynamical behavior variation of the workpiece with respect to the tool position or tool tip node was investigated. Thevenot et al. [18], Tang et al. [19], and Song et.al. [20] had constructed a three-dimensional stability lobe diagram of the spindle speed, axial depth, and tool position with a constant radial depth. In this study, an algorithm was designed for automatically trimming the intersected line between stable and unstable zones occurring in a 2D or 3D lobe diagram. This study addresses the changes to system dynamic performances caused by changes in the position of the worktable. The concept is seldom found in other literatures except in ref. [11].

2.6 The PSO algorithm [21]

Particle swarm optimization (PSO) is a population-based stochastic optimization technique developed by Eberhart and Kennedy in 1995, inspired by the social behavior of birds flocking or fish schooling. Similar to many other global optimization methods, the operation of the PSO method requires an iterative process and a proper stopping criterion. On each iteration in the PSO method, each particle's current velocity is updated based on the particle's previous velocity, the particle's position vector relative to its best location, and position vector relative to the global best location. Then, each particle's position is updated using the particle's new velocity. In mathematical terms, the two equations describing the movement of a particle in an iteration are:

$$v(t+1) = w\,v(t) + c_1 r_1(p(t) - x(t)) + c_2 r_2(g(t) - x(t)) \tag{15}$$

$$x(t+1) = x(t) + v(t+1) \tag{16}$$

Equation 15 updates a particle's velocity. The term $\boldsymbol{v}(t+1)$ means the velocity of the particle at time $t+1$ or at $t+1$ iterations. Notice that $\boldsymbol{v}$, $\boldsymbol{p}$, $\boldsymbol{g}$, and $\boldsymbol{x}$ are vectors. The velocity of a particle depends on three components. The first term is $w\ \boldsymbol{v}(t)$. The factor w is called the inertia weight and is a constant to be defined; $\boldsymbol{v}(t)$ is the velocity at time t. The second term is $c_1\ r_1\ (\boldsymbol{p}(t)-\boldsymbol{x}(t))$. The c_1 is a constant called the cognitive (or personal or local) weight. r_1 is a random variable in the range [0, 1]. $\boldsymbol{p}(t)$ is the particle's best position found so far. $\boldsymbol{x}(t)$ is the particle's current position. The third term in the velocity update equation is $c_2\ r_2\ (\boldsymbol{g}(t)-\boldsymbol{x}(t))$. c_2 is a constant called the social or global weight. r_2 is a random variable in the range [0, 1]. $\boldsymbol{g}(t)$ is the global best position found by any particle in the swarm so far. Once the new velocity, $\boldsymbol{v}(t+1)$, has been determined, it is used to compute the new particle position $\boldsymbol{x}(t+1)$ by Eq. 16.

3 System performance analysis

3.1 The setting of basic parameters and system simulation

In this study, the data were adopted from the prototype M8620 crankshaft grinder with excellent results achieved [14]. The values of parameters for the simulated spring constants of the substructural interface, substructural masses, substructural moments of inertia, and various corresponding lengths are shown in Tables 1, 2, 3, and 4. After checking the response of the original model, the length d is equal to 0.00539 m at position L_z=0. The damping coefficient of the interface is temporarily set in accordance with known values from relevant data. Now, the coefficient is set as $[C] = \beta \times [K] = (1.0 \times 10^{-5}) \times [K]$, the equivalent model damping ratios can be computed as 0.0987 % (32.74 Hz), 0.113 % (36.73 Hz), 0.1594 % (51.07 Hz), 0.3121 % (127.08 Hz), 0.5003 % (173 Hz), 1.1906 % (379.1 Hz), and

Table 1 The spring constants (9.8×10^6N/m) of substructural interface

k_1	k_2	k_3	k_4	k_5	k_6	k_7	k_8
5.9	19.3	84.4	1.2	0.69	8.4	15.3	0.66

Table 2 The masses (in kilogram) of substructures

m_1	m_L	m_R	m_2	m_3	m_h	m_s	m_4
1,273	90.5	46.6	52.4	36	788	733	1,680

1.5316 % (487.59 Hz). This agrees with the general belief that the logarithmic decrement is near or less than 0.3 for a machine tool structure [22]. However, the actual stiffness and damping characteristics of the interface vary with several factors such as the selected types of bearings and ball screw, the values of assembly preload, the processing methods, and the joint surface. The actual stiffness and damping characteristic of the interface should be obtained by further experimental verification.

The numerical simulation is performed using the above parameters. Figure 3 shows the Nyquist plots of the system dynamic compliance in various worktable positions. When the movable worktable is located at L_z=0 and c_8=0, |MNRPODC| is 2.66×10^{-6}m/N. When the movable worktable is located at L_z=0 and c_8=0.66×98 Ns/m, |MNRPODC| is 2.08×10^{-6}m/N. When the movable worktable is located at L_z=−0.2 m and c_8=0.0, |MNRPODC| is 2.83×10^{-6}m/N. When the movable worktable is located at L_z=0.2 m and c_8=0.0, |MNRPODC| is 2.19×10^{-6}m/N. It is noticed that when the values of parameters L_z or c_8 are changed, a significant change to the system dynamic performance can occur.

3.2 The effect of *d* on MNRPODC

As d increases from 0 to 16.2 cm, it is seen that the natural frequencies of the system in the numerical analysis have changed slightly (mainly in the first three natural frequencies), but the MNRPODC performance curve does not change within $-0.65\ \text{m}\le L_z\le 0.3$ m as Fig. 4. Therefore, with the prototype assembly, the distance between the mass center of the workpiece and the worktable module in the z direction has little effect on the cutting stability.

3.3 Static stiffness analysis

When the static stiffness k_s between the tool and the workpiece is computed at a location (L_z), no inertia force and damping force are involved. That means that ω=0.0 in Eq. 3, and the equation of motion becomes

$$[K]_{7\times7}\{x\}_{7\times1} = \{f\}_{7\times1}e^{j\omega t}.$$

The compliance between the tool and the workpiece can be expressed as

$$\begin{aligned}\{r(t)\}_{1\times1} &= 1/k_s = (x_2 - L_{2L}\times\theta_2) - (x_3 - L_Z\times\theta_3)\\ &= \{f\}^T_{1\times7}\{x\}_{7\times1} = \{f\}^T_{1\times7}[K]^{-1}_{7\times7}\{f\}_{7\times1.}\end{aligned} \tag{17}$$

The correlation between the k_s and L_z for various k_8 is shown in Fig. 5. It can be seen that the system static stiffness is different at various locations with changing k_8. The static compliance from the prototype parameters at location L_z=0.0 is the value of 2.656 $times10^{-8}$ m/N $\left(1/k_s = 1/1.768\ \ times10^7\ m/N\right)$, which is the sum of mode compliance at all natural modes. No matter how much k_8 changes, the greatest system stiffness occurs at location L_z= 0.2 m since the stiffness k_4 is greater than k_5.

3.4 The MNRPODC performance

When the initial sets of parameters with c_8=0.0 are used, the relationship among the natural frequencies, MNRPODC and frequency emerge at MNRPODC in various worktable positions, is illustrated in Fig. 6. The MNRPODC curve for the working range from −0.6 to 0.338 m shows an upward concave shape. Near the position L_z=−0.2 m, the curve is shown with the minimum value of -2.832×10^{-6}m/N. This occurs at the frequency of 129.8 Hz, close to the fourth natural frequency. At this position, the second natural frequency is very close to the first natural frequency owing to the coupling effect. The remaining parts of the MNPRODC curve range from 0.338 to 0.6 m, increasing gradually to the ends with all emerging frequencies close to the first natural frequency.

3.5 Chatter stability lobes

It is assumed that the hard spots in the material would cause a regenerative chatter effect as the previously mentioned theory proposed. When the stability lobe is calculated by Eq. 14, the cutting force coefficient of 1035 carbon steel K_f is 2.3×10^9N/m^2, the prototype parameters with c_8=0.0 are adopted. The 3D stability lobe for $(, b_{\lim}, L_z)$ is shown in Fig. 7. The top part of the surface is the chatter zone. The bottom part is a stability zone. A detailed discussion of the lobe diagrams states as follows:

1. Figure 8 shows the 3D view of stability lobe diagram along the L_z direction. In that figure, the critical value of

Table 3 The moments of inertia (in kilograms times meter square) of substructures

J_2	J_3	J_4
27.13	1.67	3,827.7

Table 4 The corresponding lengths (in centimeter) of substructures

L_{12}	L_{13}	L_{22}	L_{23}	L_{2L}	L_{2R}	L_{34}	L_{35}	L_{44}	L_{45}	L_{4h}	L_{4s}	L_L	L_R
27.25	27.25	17.802	36.698	32.802	52.798	71.5	70.75	70.961	71.289	102.46	102.04	112.5	118.5

$b_{\lim}$ is 0.077 mm and the position of the worktable ranges from −0.65 to 0.65 m. In an absolutely stable zone, no chatter will be present at any spindle speed. That is the reason that near the position L_z=−0.2 m where the MNRPODC is minimized, and the value is 2.832×10^{-6}m/N. The $b_{\lim,cr}$ can be directly obtained from $b_{\lim,cr} = 1/\left(2\cdot K_f\cdot|MNRPODC|\right)$ in the traverse positions of the worktable.

2. If the spindle is operated at low speed, the worktable position is limited within −0.5 m≤L_z≤0.35 m. No chatter occurs when the spindle is running at Ω=120 Hz with a maximum of $b_{\lim}$ of 1.0 mm. In this case, the $b_{\lim}$ should be 12 times as that in an absolutely stable zone (zone A in Fig. 9).
3. If the spindle is operated at high speed, the worktable position is limited within −0.5 m≤L_z≤0.35 m. No chatter occurs when the spindle is running at Ω=120 Hz with a maximum of $b_{\lim}$ of 3.7 mm. In this case, the $b_{\lim}$ should be 48 times as that in an absolutely stable zone (zone B in Fig. 9).

3.6 Grinding time domain simulation [12, 13, 16]

Time domain simulation is an alternative method for determining regenerative chatter. The machining forces and structural vibrations are simulated in the time domain for a specific set of process parameters. The forces and displacements are examined to determine if chatter is present. A time domain simulation in this study is executed as follows: (1) the instantaneous chip thickness is determined using the current and previous tool vibrations; (2) the cutting force is calculated; (3) the force is used to find the new displacement; and (4) the process is repeated in small time steps. The machining force is calculated using Eq. 10 and the displacement is calculated

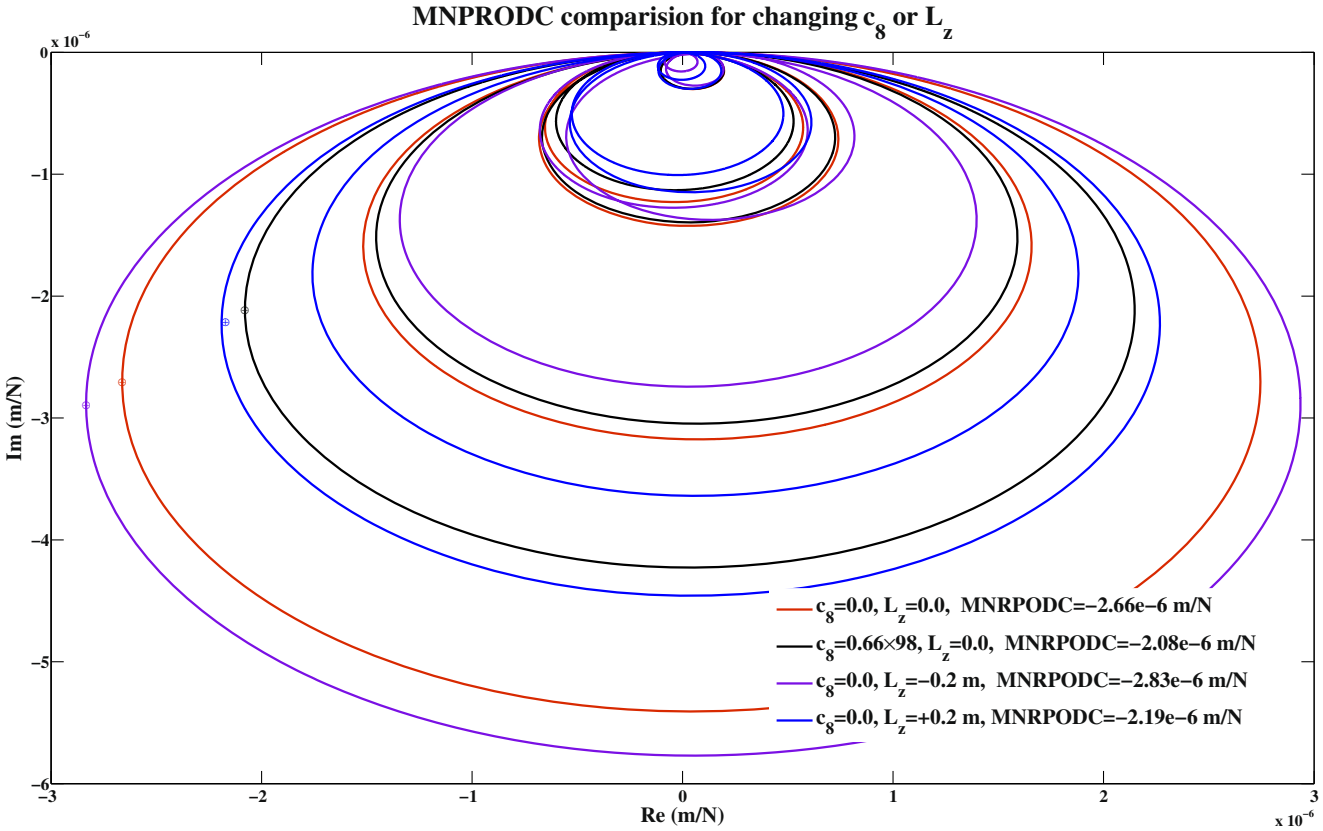

Fig. 3 The Nyquist plots of the prototype with different c_8 and L_z

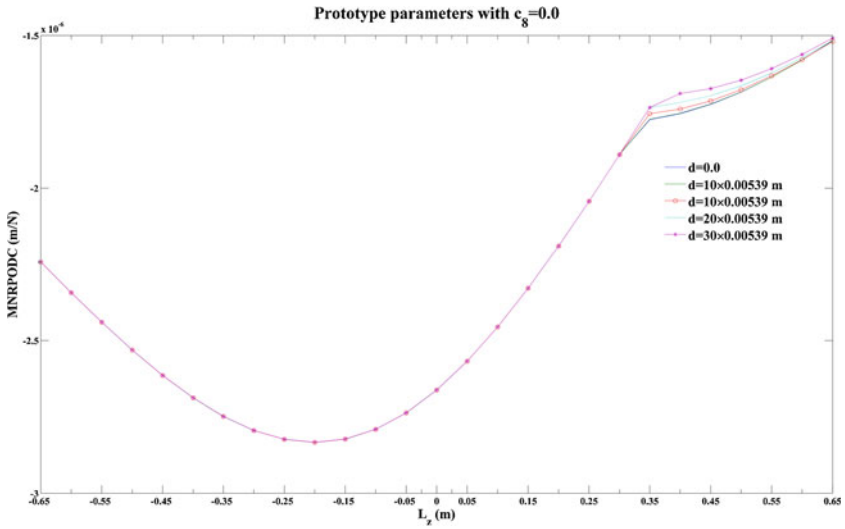

Fig. 4 The correlation between the MNRPODC and L_z for various d

using Eq. 13. Both incorporate the numerical technique of Eq. 8. In the following section, some time domain simulations are demonstrated to validate the lobe diagram.

When the aforementioned system parameters with c_8=0.0 are used, the corresponding 2D stability lobe diagram at L_z=−0.2 m is shown in Fig. 10. In this figure, point B is located in the stability zone, but both points A and C are located at the chatter zone. Applying the time domain simulation, the force and tool displacement near the stability thresholds can be determined (Fig. 10). Figure 11 shows the results (point A) of

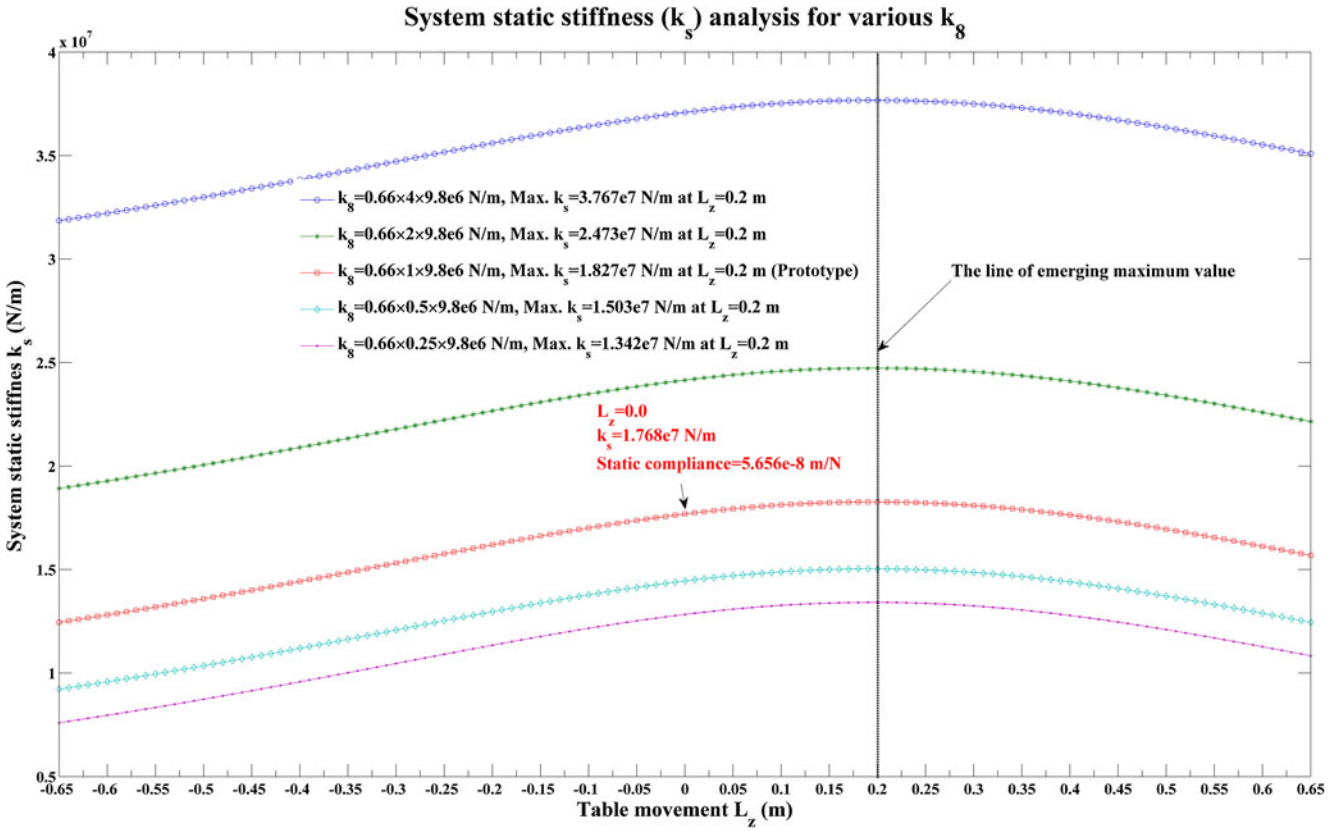

Fig. 5 The correlation between the k_s and L_z for various k_8

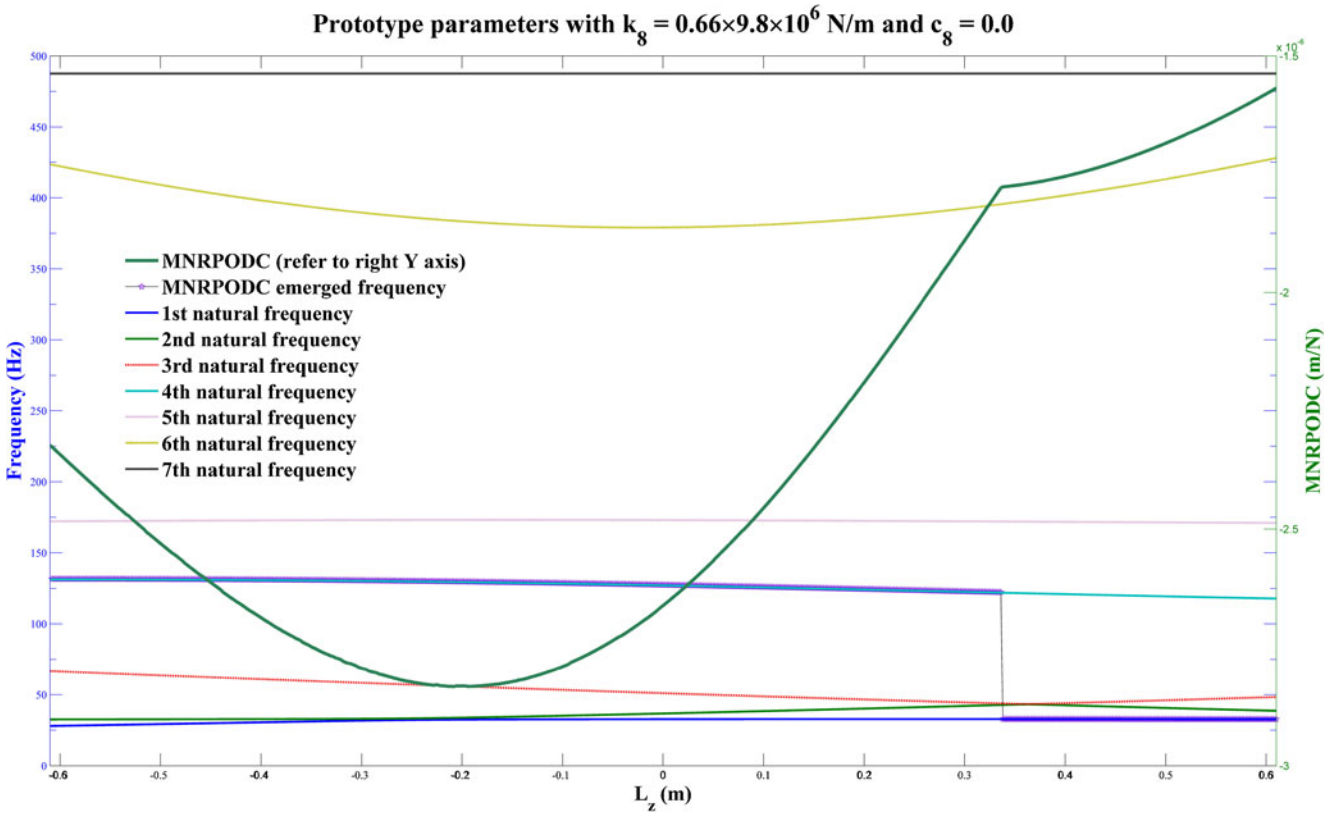

Fig. 6 MNRPODC, natural frequencies, and MNRPODC-emerged frequency, as a function of L_z

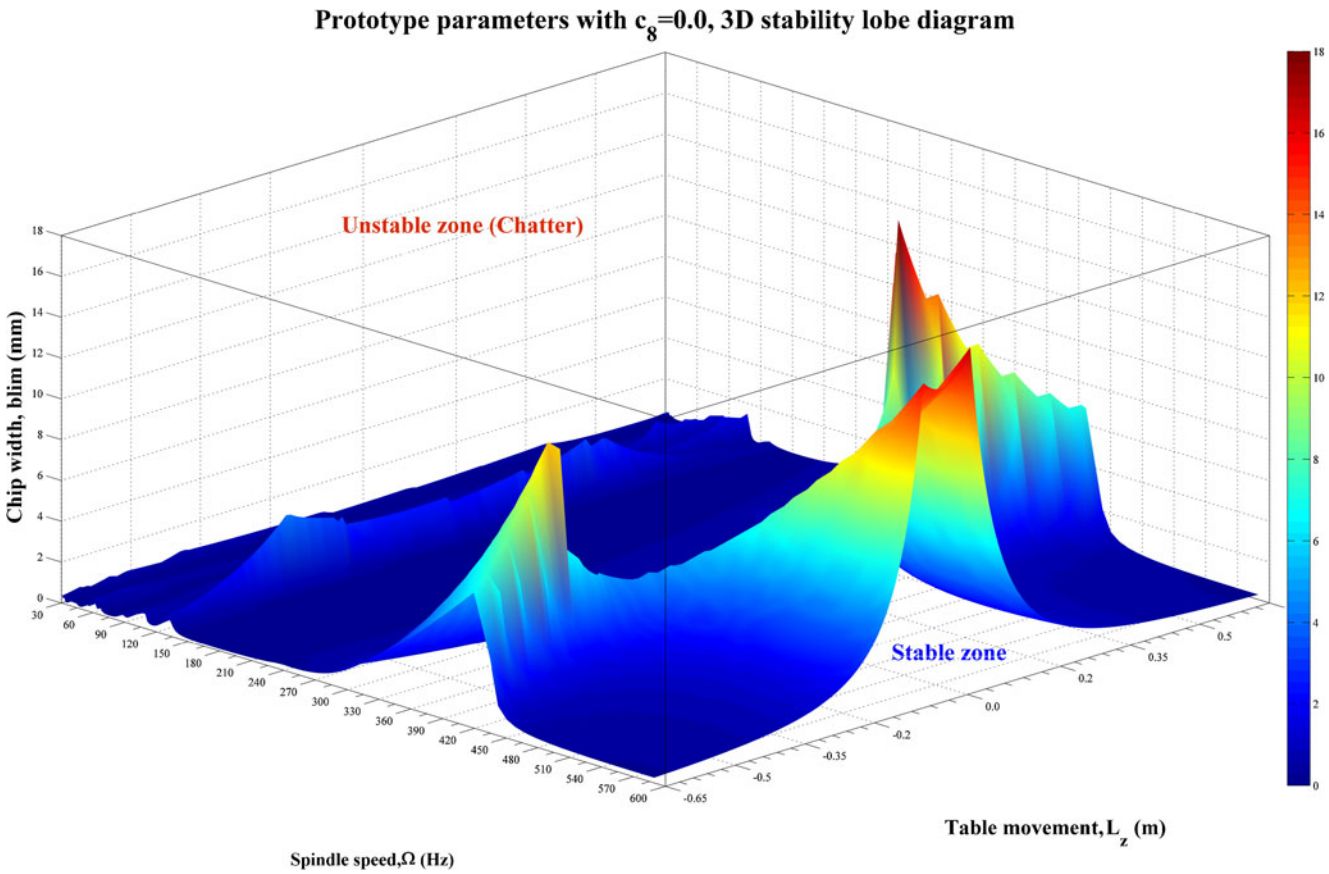

Fig. 7 Three-dimensional stability lobe diagram for $\Omega - b_{\lim} - L_z$

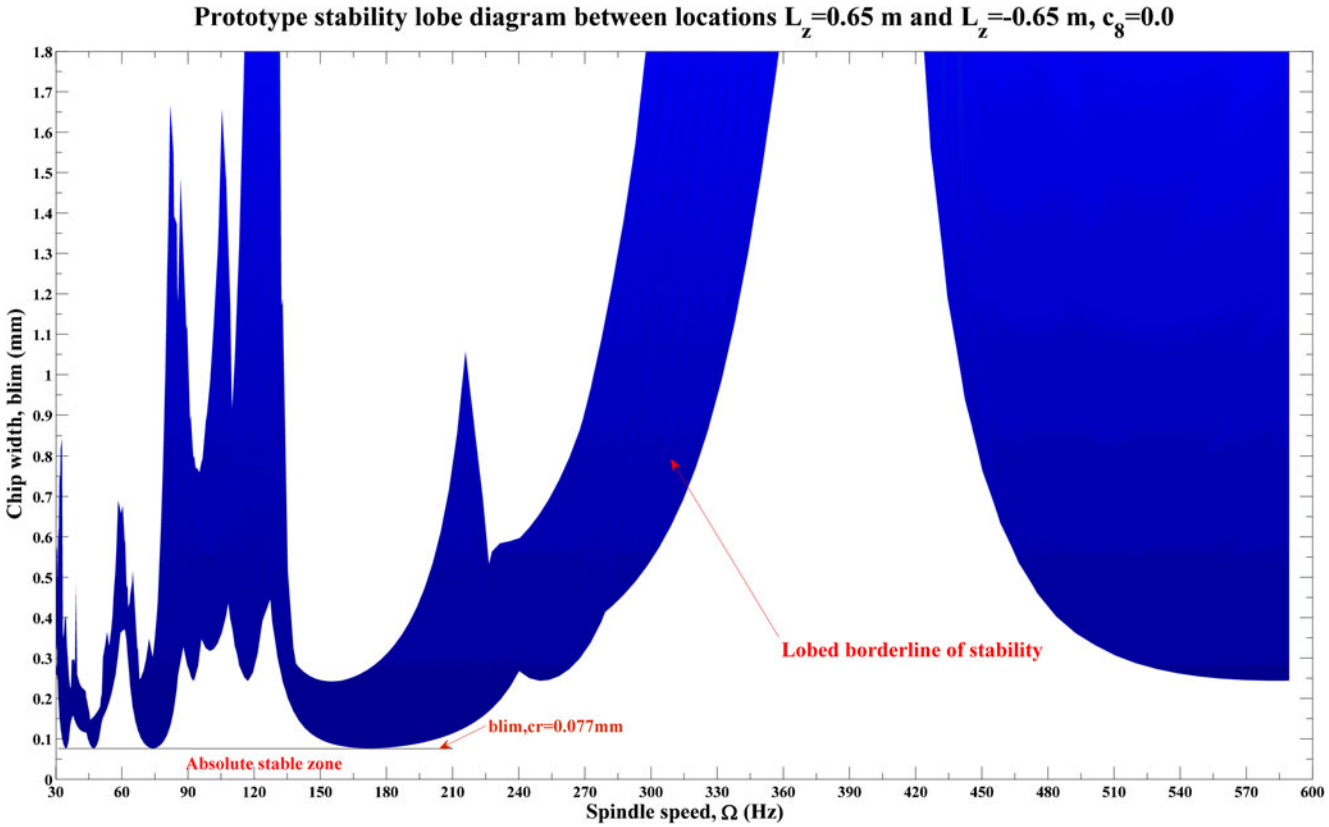

Fig. 8 3D view of stability lobe diagram along L_z direction for the prototype with parameters under worktable movement range ($-0.65\ \text{m} \leq L_z \leq 0.65\ \text{m}$)

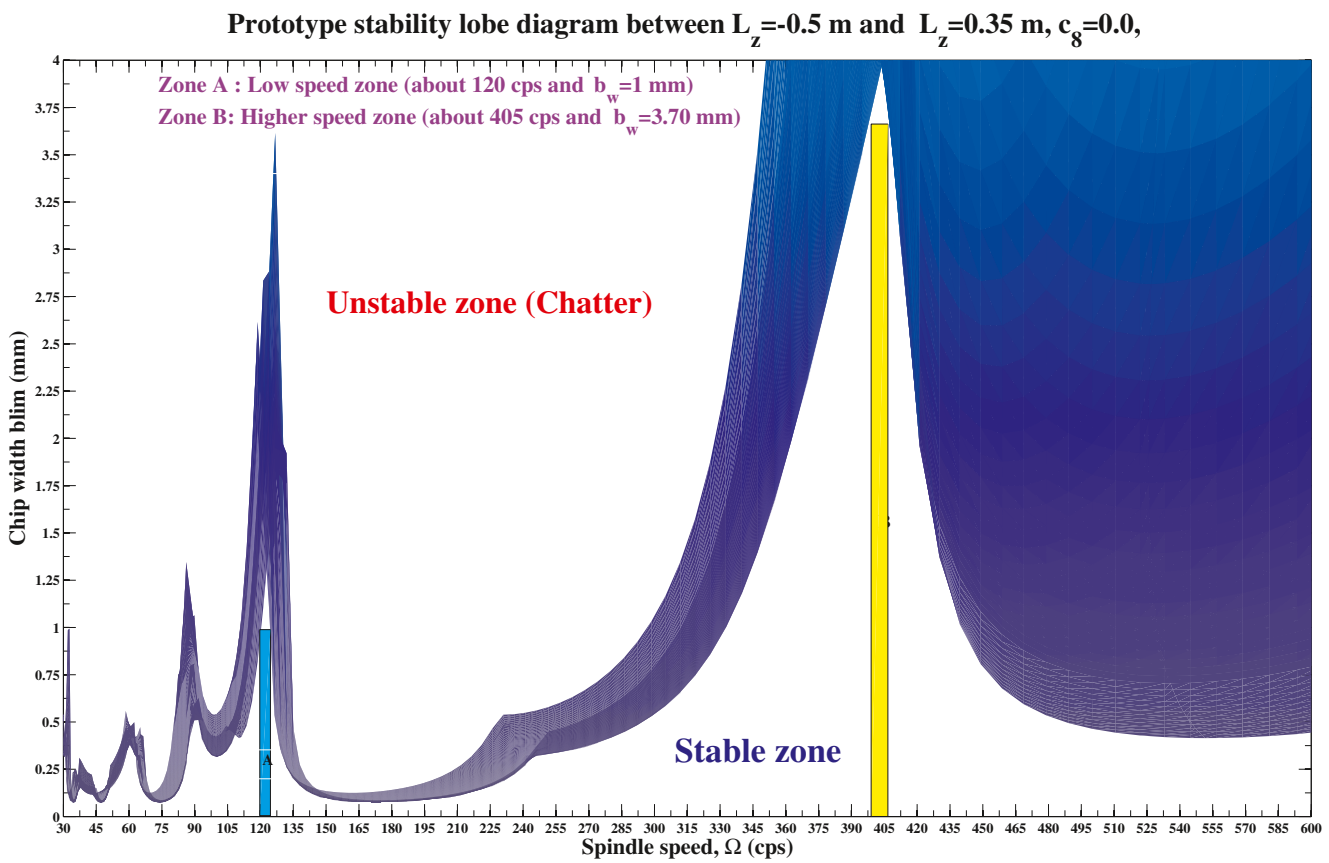

Fig. 9 3D view of stability lobe diagram along the L_z direction for the prototype with parameters under worktable movement range ($0.5\ \text{m} \leq L_z \leq 0.35\ \text{m}$)

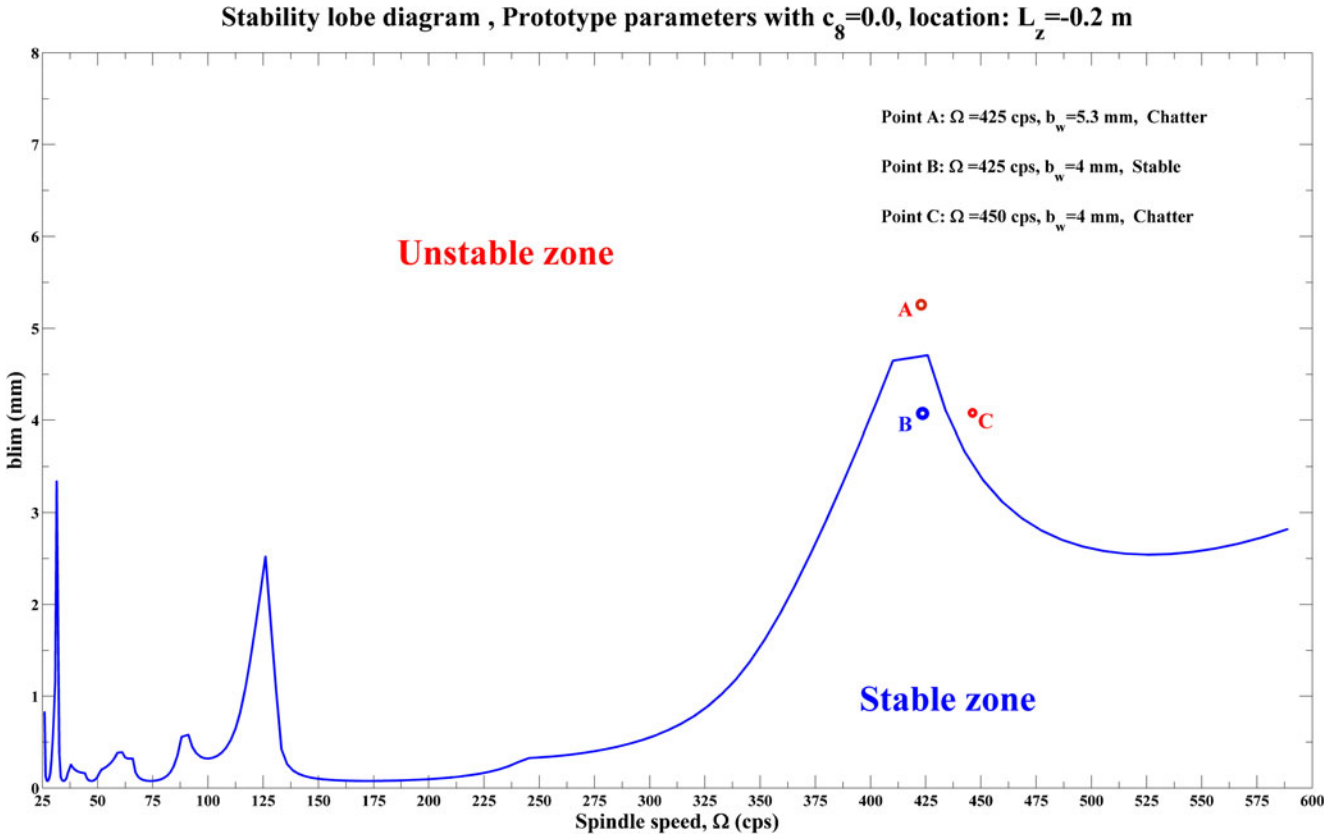

Fig. 10 Stability lobe diagram at location L_z=−0.2 m

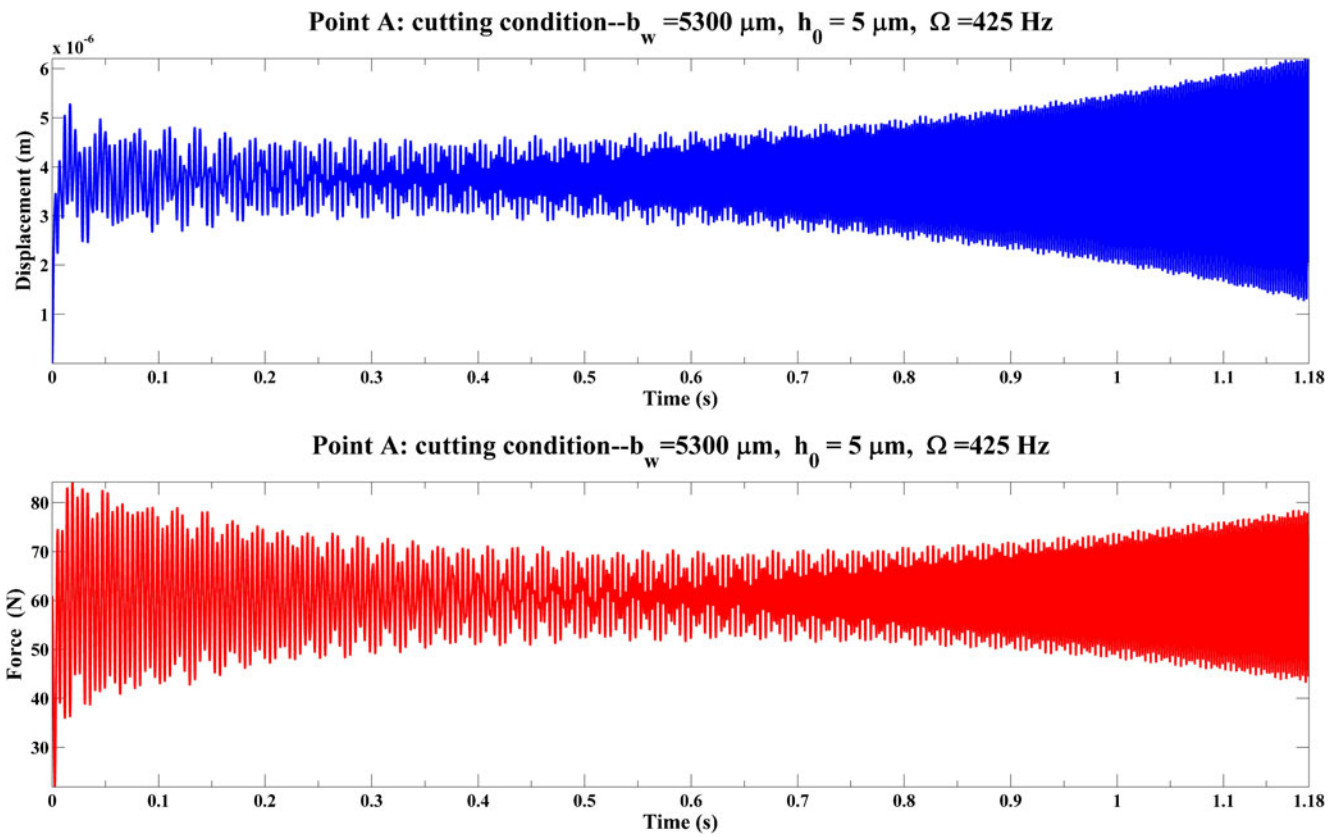

Fig. 11 Time domain displacement and force for b_w=5.3 mm, h_0=5 μm, and Ω=425 Hz (unstable point A in Fig. 10)

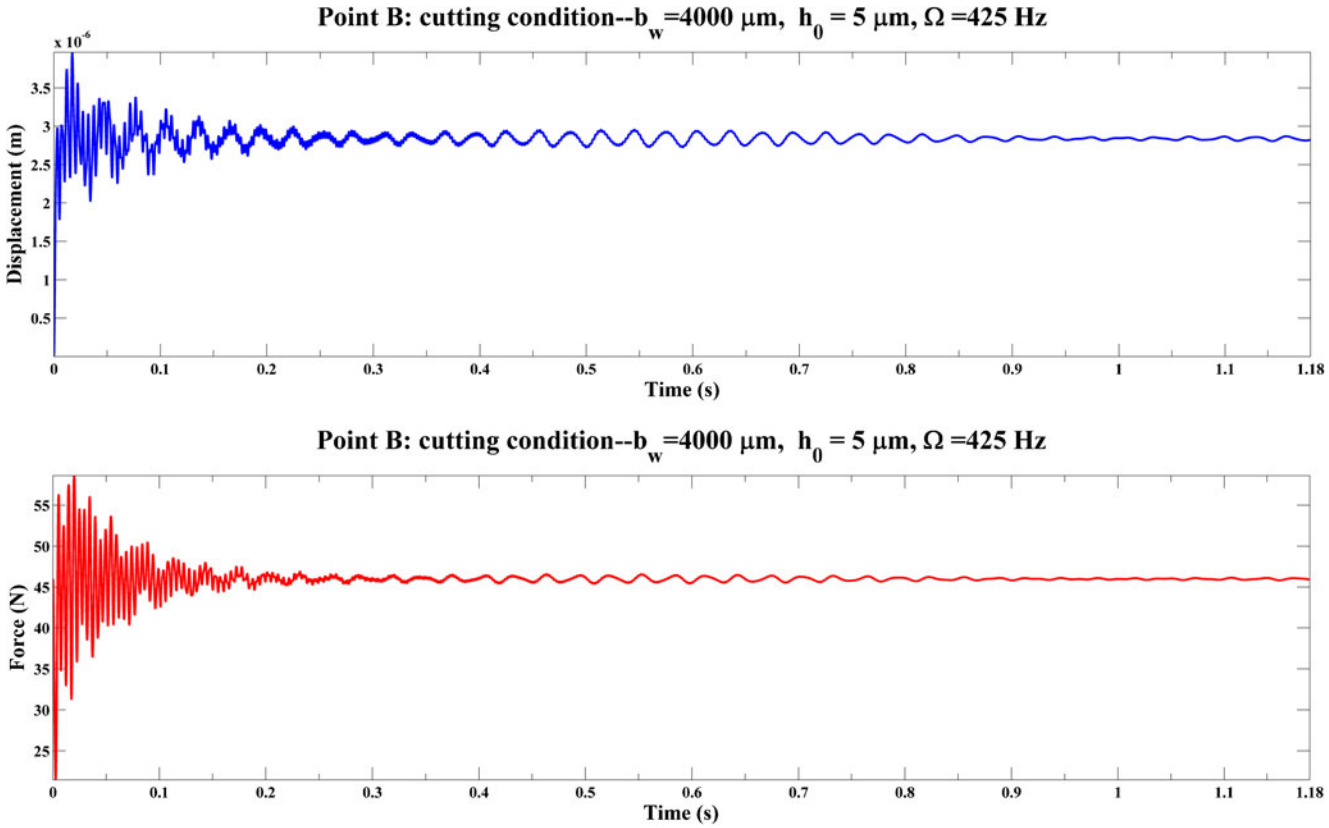

Fig. 12 Time domain displacement and force for b_w=4 mm, h_0=5 μm, and Ω=450 Hz (stable point B in Fig. 10)

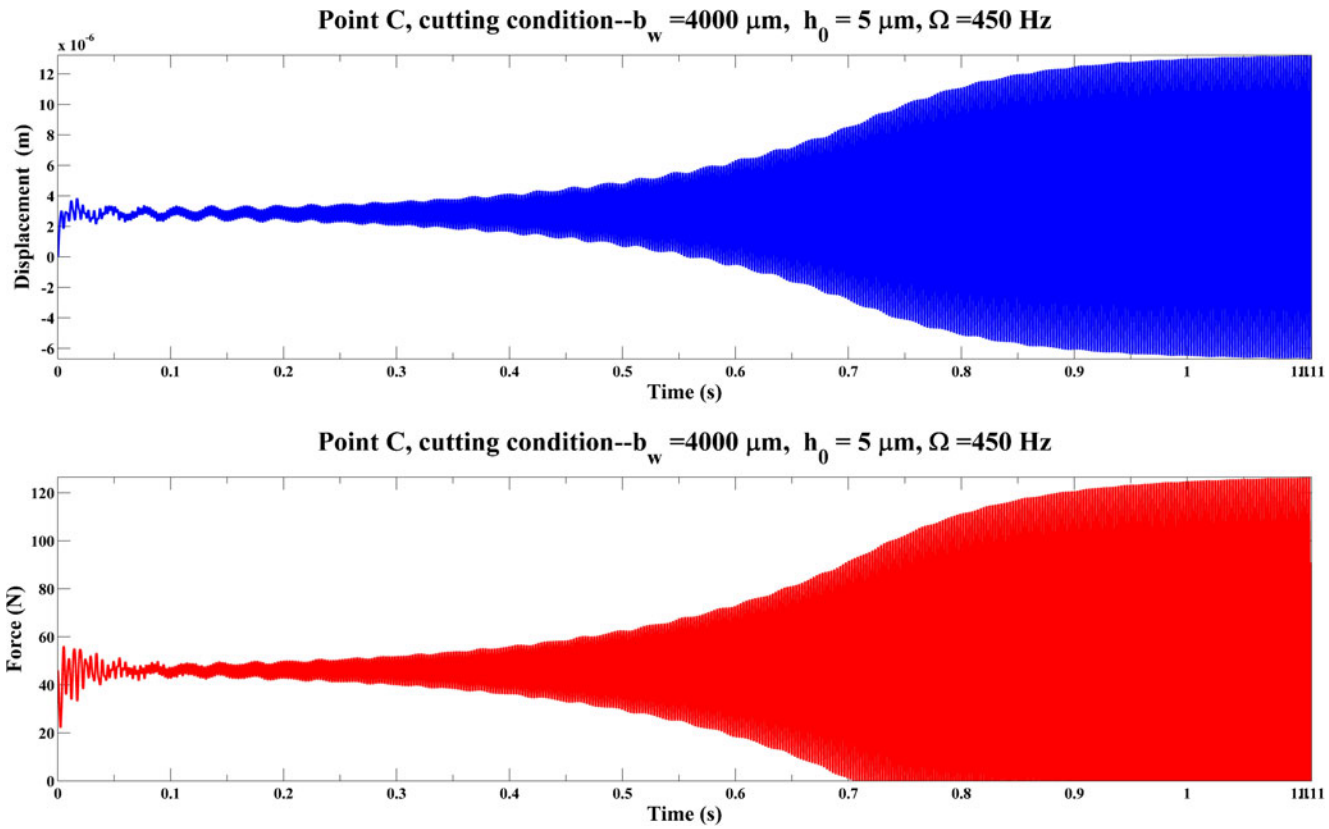

Fig. 13 Time domain displacement and force for b_w=4 mm, h_0=5 μm, and Ω=450 Hz (unstable point C in Fig. 10)

Table 5 The summaries of optimal search result by the PSO method (Prototype parameters with c_8=0.0 and [*C*]=1.0*E*−5×[*K*])

Case study	MNPRODC	Improved factor	Design variables (range)			
			k_2 (10~30)	k_8 (0.055~5.335)	k_4 (0.1~9.7)	k_5 (0.0575~5.5775)
Prototype	–0.000002832	1.00	19.3	0.66	1.2	0.69
PSO_run1 (optimum)	–4.3753E−07	6.4728	10	5.335	7.039	2.9313
PSO-run2	–4.3795E−07	6.4665	10	5.335	7.099	2.9347
PSO-run3	–4.4234E−07	6.4023	10	5.335	5.3343	3.1465
PSO-run4	–4.3787E−07	6.4677	10	5.335	8.0232	2.8668
PSO-run5	–4.3804E−07	6.4652	10	5.335	8.2281	2.8674

the conditions of b_w=5.3 mm, h_0=5 μm, and Ω=425 Hz. The force and displacement values are increasing significantly after 0.7 s. On the other hand, Fig. 12 shows the results (point B) of the conditions of b_w=4 mm, h_0=5 μm, and Ω=425 Hz. The force and displacement values are decreasing significantly with time within 0.2 s. Figure 13 shows the results (point C) of the conditions of b_w=4 mm, h_0=5 μm, and Ω=450 Hz. The force and displacement are increasing significantly after 0.3 s. From these results, the correctness of the stability lobe diagram is verified. Moreover, the strategy of decreasing the b_{lim} or increasing spindle speed Ω is confirmed as a good way to suppress chatter.

3.7 Optimization analysis

The factors (k_2, k_4, k_5, and k_8) of the crankshaft grinding machine can be determined by the energy balance principle or sensitivity analysis. When the worktable is in different positions, the improved system dynamic performance and the optimum design can be described as follows:

$$Maximize: \left(|MNRPODC|_{prototype} - |MNRPODC|_{prototype\ improved}\right)$$

$$s.t. \quad 10 \le k_2 \le 30, \quad 0.1 \le k_4 \le 9.7;$$

$$0.0575 \le k_5 \le 5.5775, \ 0.055 \le k_8 \le 5.335;$$

The unit of k is 9.8×10^6 N/m;
within $-0.65m \le L_z \le 0.65\ m$.

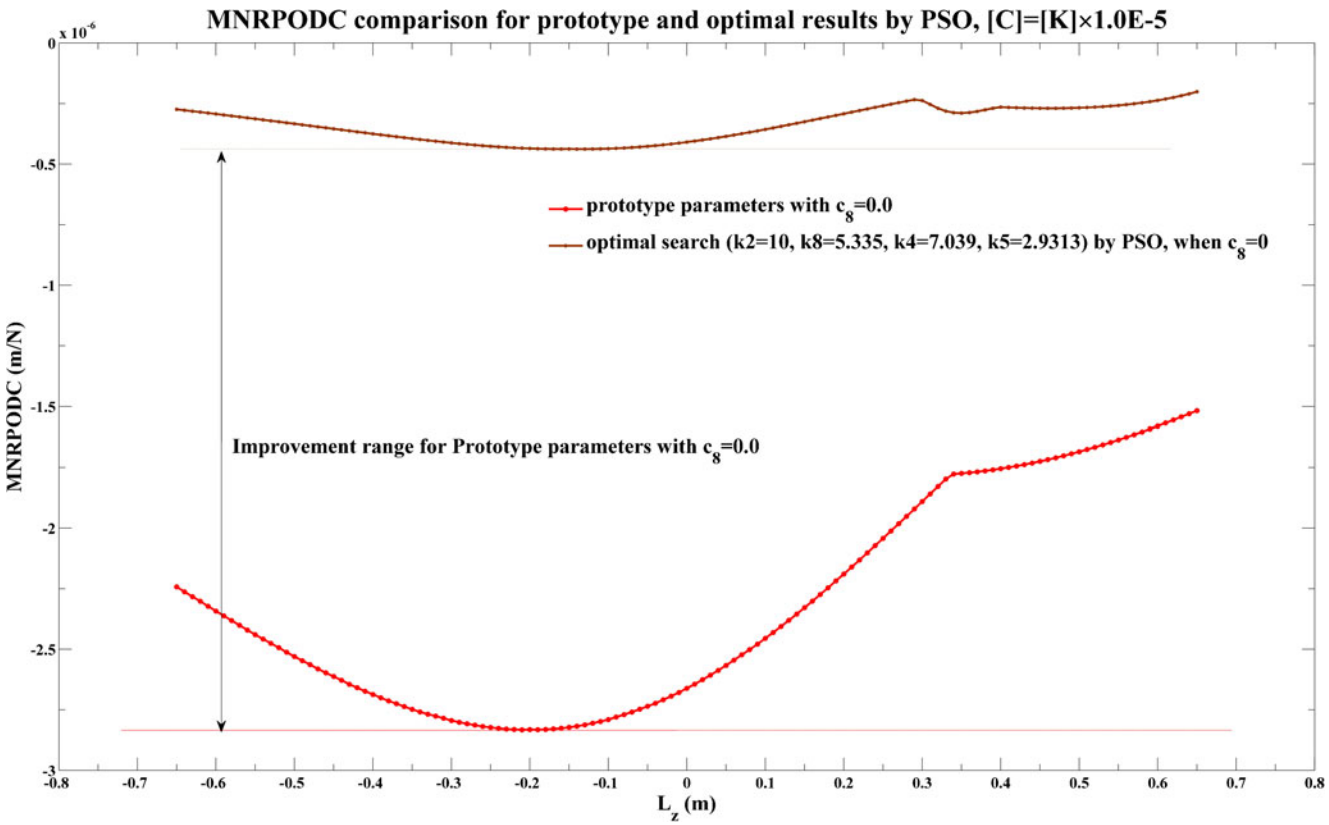

Fig. 14 Comparison of MNRPODC performance for various positions between the optimal design and prototype

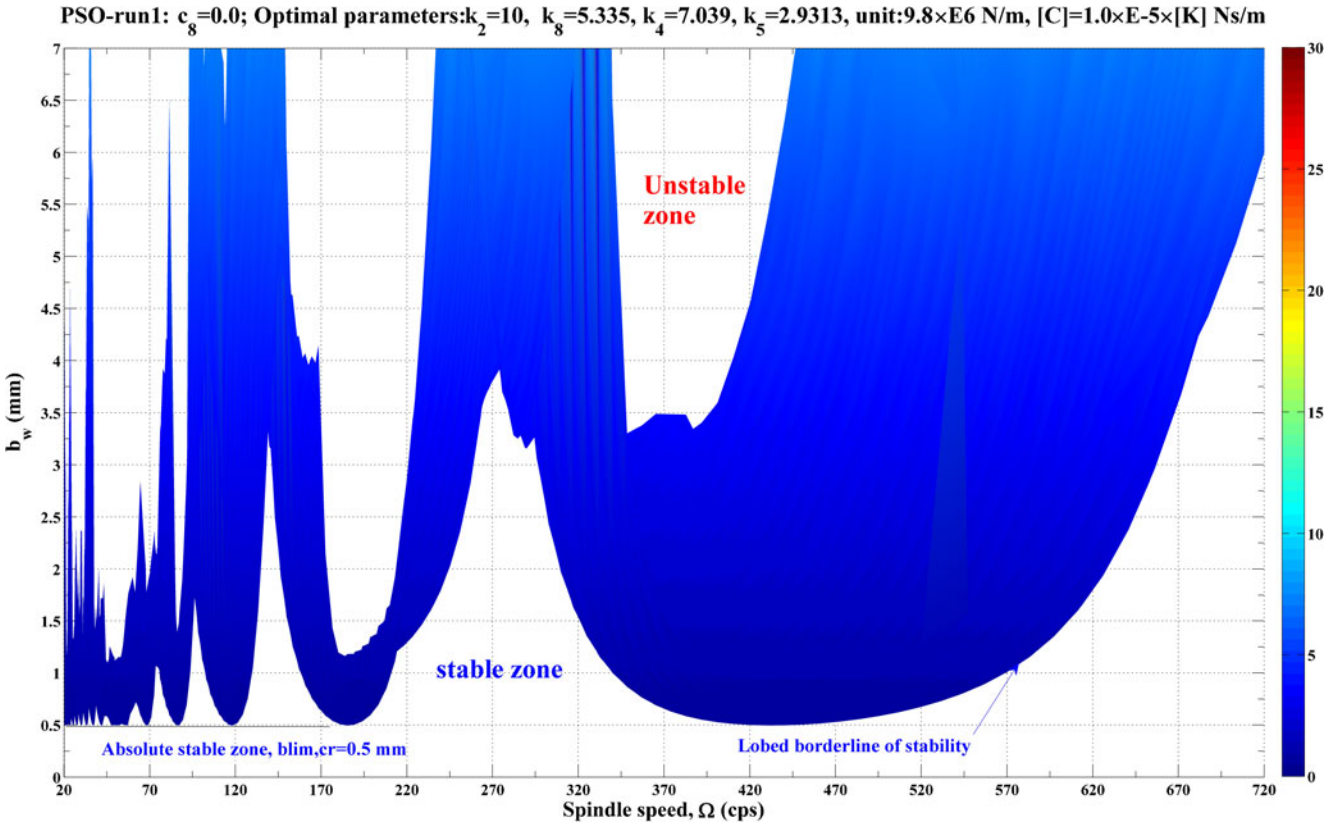

Fig. 15 3D view of the stability lobe diagram along the L_z direction for the optimal case under worktable movement range ($-0.65\ \text{m} \le L_z \le 0.65\ \text{m}$)

The case of c_8=O, in the form of $[C]=10^{-5}\times[K]$ Ns/m, is considered in the optimization analysis. Here, the prototype values of $|MNRPODC|$ is 2.832×10^{-6}m/N. PSO parameters for this case is set by (1) swarm size=20, (2) maximum velocity of particle=4, (3) inertia weight=0.9 (static), (4) local weight (self-confidence)=2, (5) global weight (swarm confidence)=2, (6) maximum iterations=200 epochs, (7) minimum global error gradient=1.0×10^{-8}, and (8) epochs before error gradient criterion terminates run=50.

Through several runs by the PSO method, Table 5 is the summary of optimal results for these cases. It was found that the best values of $|MNRPODC|$ are 4.3753×10^{-7}m/N compared to the 2.832×10^{-6}m/N value of the prototype, an improvement factor of approximately 6.5 and the corresponding design variables were k_2=10, k_4=1.2, k_5=2.9313, and k_8=5.335. The unit of k is 9.8×10^{6}N/m. The performance curves of MNRPODC in various positions are compared between the optimal design and prototype for this case as shown in Fig. 14. The 3D view of stability lobe diagram along the L_z direction for the best value is shown in Fig. 15. It shows that the regardless of the spindle speed, the limiting critical chip width increases from 0.077 mm of prototype to 0.5 mm after optimization, an improvement factor of approximately 6.5.

4 Conclusions

Based on the results obtained in this study, the following conclusions are made:

1. The MNPRODC curve for the working which ranges from −0.6 to 0.338 m shows an upward concave curve. Near the position L_z=−0.2 m, the curve with the maximum value of $|MNRPODC|$ is generated, but the structural performance here is the worst among all the tested cases. At this position, the second natural frequency is very close to the first natural frequency owing to the coupling effect. This is the main cause of decreased limiting critical chip width.
2. An increase of k_8 and c_8 will improve the machine stability which is indicated by the value of corresponding $|MNRPODC|$. For any spindle speed, the $b_{\text{lim,cr}}$ can be easily calculated by using the equation $b_{\text{lim,cr}}=1/(2\cdot K_f\cdot|\text{MNRPODC}|)$ in the traverse positions of the worktable. Therefore, a large value of $b_{\text{lim,cr}}$ is recommended in practical applications.
3. In the case of the prototype assembly, the distance between the mass center of the workpiece and the worktable module in the z direction has little effect on the cutting stability. It means that the lines of the center of

gravity of the workpiece and the worktable module along x direction do not need to be collinear.

4. The curves for k_s and L_z are parabolic, when k_8 has a fixed value. Regardless of whether k_8 changes, the greatest static stiffness occurs at location L_z=0.2 m since here the movement parts include two layers (the workpiece and the worktable module) and the stiffness k_4 is greater than k_5 in the model. This is different from the constant static stiffness analysis in various positions for a surface grinder model [11].
5. Based on the regenerative chatter model and stability theories, a program for producing a three-dimensional stability lobe diagram for the multi-DOF machine system is developed which can automatically trim the unnecessary line-crossing issues between the stable and chatter regions. Meanwhile, by using the time domain analysis, the predictable response within a short period of time can be attained. The method can also be used to verify the stability lobe diagrams.
6. In the optimization analysis, the limiting critical chip width ($b_{\mathrm{lim,cr}}$) can be increased from 0.077 mm in the prototype machine to 0.5 mm when the optimal design variables are used. With a factor of 6.5, quality improvement is obtained. It also shows that the larger the value of k_8, the smaller the $|MNRPODC|$ will be in various worktable positions.

Acknowledgments This study is supported by the National Science Council of Taiwan, contract no. NSC 99-2221-E-182-022. We also thank a good friend, Tan, Shen Hsiao, working at the research institutes in Singapore to carry out full-scale polishing to make the article more complete and readable.

References

1. Tobias SA, Fishwick W (1958) The chatter of lathe tools under orthogonal cutting conditions. Trans ASME 80:1079–1088
2. Tlusty J, Polacek M (1963) The stability of machine tool against self excited vibrations in machining. ASME Production Engineering Research Conference, Pittsburgh, pp 465–474
3. Koenigsberger F, Tlusty J (1970) Machine tool structure. Pergamon, London
4. Altintas Y, Budak E (1995) Analytical prediction of stability lobes in milling. Ann CIRP 44(1):357–362
5. Tlusty J, Ismail F (1981) Basic nonlinearity in machining chatter. Ann CIRP 30:21–25
6. Schmitz TL (2002) Automatic trimming of machining stability lobes. Int J Mach Tool Manuf 42:1479–1486
7. Yoshimura M (1976) Analysis and optimization of structural dynamics of machine tools by a synthesis of dynamic rigidity program system. *Preceedings of the 16th International Machine Tool Design and Research Conference*, pp. 209–215
8. Yoshimura M (1977) Study on optimum design of machine structures with respect to dynamic characteristics. Bull Jpn Soc Mech Eng 145(20):811–818
9. Altintas Y, Weck M (2004) Chatter stability of metal cutting and grinding. CIRP Ann Manuf Technol 53(2):619–642
10. Hwang RM, Cha KC (2008) Construction of a prediction model for the structural stability of a surface grinder using backpropagation neural wetwork. Int J Adv Manuf Technol 37:1093–1104
11. Cha KC, Wang N, Liao JY (2011) Dynamics and stability analysis of the simplified model for the surface grinder in various worktable positions. J Multi-body Dynamics 225:220–234
12. Tlusty G (2000) Manufacturing processes and equipment. Prentice Hall, Upper Saddle River
13. Schmitz TL, Smith KS (2009) Machining dynamics: frequency response to improved productivity. Springer, New York
14. Zhang BS, Zhang S (1986) Optimization of structural parameters of crank shaft grinding machine M8260. J of Gansu U of Technol 12(4):89–101
15. Gawronski W (1998) Dynamics and control of structures: a modal approach. Chap 2. Springer, New York
16. Altintas Y (2000) Manufacturing automation: metal cutting mechanics, machine tool vibrations, and CNC design. Cambridge University Press, New York
17. Tarng YS, Hseih YW, Li TC (1996) Automatic selection of spindle speed for suppression of regenerative chatter in turning. Int J Adv Manuf Technol 11:12–17
18. Thevenot V, Arnaud L, Dessein G, Cazenave-Larroche G (2006) Integration of dynamic behaviour variations in the stability lobes method: 3D lobes construction and application to thin-walled structure milling. Int J Adv Manuf Technol 27:638–644
19. Tang A, Liu Z (2009) Three-dimensional stability lobe and maximum material removal rate in end milling of thin-walled plate. Int J Adv Manuf Technol 43:33–39
20. Song Q, Ai X, Tang W (2011) Prediction of simultaneous dynamic stability limit of time–variable parameters system in thin-walled workpiece high-speed milling processes. Int J Adv Manuf Technol 55:883–889
21. Kennedy J, Eberhart R (1995) Particle swarm optimization. Proc IEEE Int Conf Neural Net, Perth, Australia 1942–1945
22. Harris CM, Piersol AG (2002) Harris' shock and vibration handbook, 5th edn. McGraw-Hill, New York